



# A theoretical and numerical study of a phase field higher-order active contour model of directed networks

Aymen El Ghoul, Ian Jermyn, Josiane Zerubia

## ► To cite this version:

Aymen El Ghoul, Ian Jermyn, Josiane Zerubia. A theoretical and numerical study of a phase field higher-order active contour model of directed networks. The Tenth Asian Conference on Computer Vision (ACCV), Nov 2010, Queenstown, New Zealand. 2010. <inria-00522443>

**HAL Id: inria-00522443**

**<https://hal.inria.fr/inria-00522443>**

Submitted on 30 Sep 2010

**HAL** is a multi-disciplinary open access archive for the deposit and dissemination of scientific research documents, whether they are published or not. The documents may come from teaching and research institutions in France or abroad, or from public or private research centers.

L'archive ouverte pluridisciplinaire **HAL**, est destinée au dépôt et à la diffusion de documents scientifiques de niveau recherche, publiés ou non, émanant des établissements d'enseignement et de recherche français ou étrangers, des laboratoires publics ou privés.

# A theoretical and numerical study of a phase field higher-order active contour model of directed networks

Aymen El Ghoul, Ian H. Jermyn and Josiane Zerubia

ARIANA - Joint Team-Project INRIA/CNRS/UNSA  
2004 route des Lucioles, BP 93, 06902 Sophia Antipolis Cedex, France

**Abstract.** We address the problem of quasi-automatic extraction of directed networks, which have characteristic geometric features, from images. To include the necessary prior knowledge about these geometric features, we use a phase field higher-order active contour model of directed networks. The model has a large number of unphysical parameters (weights of energy terms), and can favour different geometric structures for different parameter values. To overcome this problem, we perform a stability analysis of a long, straight bar in order to find parameter ranges that favour networks. The resulting constraints necessary to produce stable networks eliminate some parameters, replace others by physical parameters such as network branch width, and place lower and upper bounds on the values of the rest. We validate the theoretical analysis via numerical experiments, and then apply the model to the problem of hydrographic network extraction from multi-spectral VHR satellite images.

## 1 Introduction

The automatic identification of the region in the image domain corresponding to a specified entity in the scene ('extraction') is a difficult problem because, in general, local image properties are insufficient to distinguish the entity from the rest of the image. In order to extract the entity successfully, significant prior knowledge  $K$  about the geometry of the region  $R$  corresponding to the entity of interest must be provided. This is often in the form of explicit guidance by a user, but if the problem is to be solved automatically, this knowledge must be incorporated into mathematical models. In this paper, we focus on the extraction of 'directed networks' (*e.g.* vascular networks in medical imagery and hydrographic networks in remote sensing imagery). These are entities that occupy network-like regions in the image domain, *i.e.* regions consisting of a set of branches that meet at junctions. In addition, however, unlike undirected networks, directed networks carry a unidirectional flow. The existence of this flow, which is usually conserved, encourages the network region to have certain characteristic geometric properties: branches tend not to end; different branches may have very different widths; width changes slowly along each branch; at junctions, total incoming width and total outgoing width tend to be similar, but otherwise width can change dramatically.

Creating models that incorporate these geometric properties is non-trivial. First, the topology of a network region is essentially arbitrary: it may have any number of connected components each of which may have any number of loops. Shape modelling methods that rely on reference regions or otherwise bounded zones in region space,

*e.g.* [1–7], cannot capture this topological freedom. In [8], Rochery *et al.* introduced the ‘higher-order active contour’ (HOAC) framework, which was specifically designed to incorporate non-trivial geometric information about the region of interest without constraining the topology. In [9], a phase field formulation of HOACs was introduced. This formulation possesses several advantages over the contour formulation. Both formulations were used to model undirected networks in which all branches have approximately the same width. While these models were applied successfully to the extraction of road networks from remote sensing images, they fail on directed networks in which branches have widely differing widths, and where information about the geometry of junctions can be crucial for successful extraction. Naive attempts to allow a broader range of widths simply results in branches whose width changes rapidly: branch rigidity is lost.

In [10], El Ghoul *et al.* introduced a phase field HOAC model of directed networks. This extends the phase field model of [8] by introducing a vector field which describes the ‘flow’ through network branches. The main idea of the model is that the vector field should be nearly divergence-free, and of nearly constant magnitude within the network. Flow conservation then favours network regions in which the width changes slowly along branches, in which branches do not end, and in which total incoming width equals total outgoing width at junctions. Because flow conservation preserves width in each branch, the constraint on branch width can be lifted without sacrificing rigidity, thereby allowing different branches to have very different widths. The model was tested on a synthetic image.

The work in [10] suffers from a serious drawback, however. The model is complex and possesses a number of parameters that as yet must be fixed by trial and error. Worse, depending on the parameter values, geometric structures other than networks may be favoured. There is thus no way to know whether the model is actually favouring network structures for a given set of parameter values. The model was applied to network extraction from remote sensing images in an application paper complementary to this one [11], but that paper focused on testing various likelihood terms and on the concrete application. The model was not analysed theoretically and no solution to the parameter problem was described.

In this paper, then, we focus on a theoretical analysis of the model. In particular, we perform a stability analysis of a long, straight bar, which is supposed to be an approximation to a network branch. We compute the energy of the bar and constrain the first order variation of the bar energy to be zero and the second order variation to be positive definite, so that the bar be an energy minimum. This results in constraints on the parameters of the model that allow us to express some parameters in terms of others, to replace some unphysical parameters by physical parameters *e.g.* the bar width, and to place upper and lower bounds on the remaining free parameter values. The results of the theoretical study are then tested in numerical experiments, some using the network model on its own to validate the stability analysis, and others using the network model in conjunction with a data likelihood to extract networks from very high resolution (VHR) multi-spectral satellite images.

In Section 2, we recall the phase field formulation of the undirected and directed network models. In Section 3, we introduce the core contribution of this paper: the theoretical stability analysis of a bar under the phase field HOAC model for directed

networks. In Section 4, we show the results of geometric and extraction experiments. We conclude in Section 5.

## 2 Network models

In this section, we recall the undirected and directed network phase field HOAC models introduced in [9] and [10] respectively.

### 2.1 Undirected networks

A phase field is a real-valued function on the image domain:  $\phi : \Omega \subset \mathbb{R}^2 \rightarrow \mathbb{R}$ . It describes a region by the map  $\zeta_z(\phi) = \{x \in \Omega : \phi(x) > z\}$  where  $z$  is a given threshold. The basic phase field energy is [9]

$$E_0^s(\phi) = \int_{\Omega} d^2x \left\{ \frac{D}{2} \partial\phi \cdot \partial\phi + \lambda \left( \frac{\phi^4}{4} - \frac{\phi^2}{2} \right) + \alpha \left( \phi - \frac{\phi^3}{3} \right) \right\} \quad (1)$$

For a given region  $R$ , Eq. (1) is minimized subject to  $\zeta_z(\phi) = R$ . As a result, the minimizing function  $\phi_R$  assumes the value 1 inside, and  $-1$  outside  $R$  thanks to the ultralocal terms. To guarantee two stable phases at  $-1$  and  $1$ , the inequality  $\lambda > |\alpha|$  must be satisfied. We choose  $\alpha > 0$  so that the energy at  $-1$  is less than that at  $1$ . The first term guarantees that  $\phi_R$  be smooth, producing a narrow interface around the boundary  $\partial R$  interpolating between  $-1$  and  $+1$ .

In order to incorporate geometric properties, a nonlocal term is added to give a total energy  $E_P^s = E_0^s + E_{NL}$ , where [9]

$$E_{NL}(\phi) = -\frac{\beta}{2} \iint_{\Omega^2} d^2x d^2x' \partial\phi(x) \cdot \partial\phi(x') \Psi \left( \frac{|x - x'|}{d} \right) \quad (2)$$

where  $d$  is the interaction range. This term creates long-range interactions between points of  $\partial R$  (because  $\partial\phi_R$  is zero elsewhere) using an interaction function,  $\Psi$ , which decreases as a function of the distance between the points. In [9], it was shown that the phase field model is approximately equivalent to the HOAC model, the parameters of one model being expressed as a function of those of the other. For the undirected network model, the parameter ranges can be found via a stability analysis of the HOAC model [12] and subsequently converted to phase field model parameters [9].

### 2.2 Directed networks

In [10], a directed network phase field HOAC model was introduced by extending the undirected network model described in Section 2.1. The key idea is to incorporate geometric information by the use, in addition to the scalar phase field  $\phi$ , of a vector phase field,  $v : \Omega \rightarrow \mathbb{R}^2$ , which describes the flow through network branches. The total prior energy  $E_P(\phi, v)$  is the sum of a local term  $E_0(\phi, v)$  and the nonlocal term  $E_{NL}(\phi)$  given by Eq. (2).  $E_0$  is [10]

$$E_0(\phi, v) = \int_{\Omega} d^2x \left\{ \frac{D}{2} \partial\phi \cdot \partial\phi + \frac{D_v}{2} (\partial \cdot v)^2 + \frac{L_v}{2} \partial v : \partial v + W(\phi, v) \right\} \quad (3)$$

where  $W$  is a fourth order polynomial in  $\phi$  and  $|v|$ , constrained to be differentiable:

$$W(\phi, v) = \frac{|v|^4}{4} + (\lambda_{22} \frac{\phi^2}{2} + \lambda_{21} \phi + \lambda_{20}) \frac{|v|^2}{2} + \lambda_{04} \frac{\phi^4}{4} + \lambda_{03} \frac{\phi^3}{3} + \lambda_{02} \frac{\phi^2}{2} + \lambda_{01} \phi \quad (4)$$

Similarly to the undirected network model described in Section 2.1, where  $-1$  and  $1$  are the two stable phases, the form of the the ultralocal term  $W(\phi, v)$  means that the directed network model has two stable configurations,  $(\phi, |v|) = (-1, 0)$  and  $(1, 1)$ , which describe the exterior and interior of  $R$  respectively. The first term in Eq. (3) guarantees the smoothness of  $\phi$ . The second term penalizes the divergence of  $v$ . This represents a soft version of flow conservation, but the parameter multiplying this term will be large so that in general the divergence will be small. The divergence term is not sufficient to ensure smoothness of  $v$ : a small smoothing term  $(\partial v : \partial v = \sum_{m,n} (\partial_m v^n)^2)$ , where  $m, n \in \{1, 2\}$  label the two Euclidean coordinates) is added to encourage this.

The divergence term, coupled with the change of magnitude of  $v$  from 0 to 1 across  $\partial R$ , strongly encourages the vector field  $v$  to be parallel to  $\partial R$ . The divergence and smoothness terms then propagate this parallelism to the interior of the network, meaning that the flow runs along the network branches. Flow conservation and the fact that  $|v| \cong 1$  in the network interior then tend to prolong branches, to favour slow changes of width along branches, and to favour junctions for which total incoming width is approximately equal to total outgoing width. Because the vector field encourages width stability along branches, the interaction function used in [9], which severely constrains the range of stable branch widths, can be replaced by one that allows more freedom. We choose the modified Bessel function of the second kind of order 0,  $K_0$  [10]. Different branches can then have very different widths.

### 3 Theoretical stability analysis

There are various types of stability that need to be considered. First, we require that the two phases of the system,  $(\phi, |v|) = (-1, 0)$  and  $(1, 1)$ , be stable to infinitesimal perturbations, to prevent the exterior or interior of  $R$  from ‘decaying’. For homogeneous perturbations, this means they should be local minima of  $W$ , which produces constraints reducing the number of free parameter of  $W$  from 7 to 4 (these are chosen to be  $(\lambda_{04}, \lambda_{03}, \lambda_{22}, \lambda_{21})$ ). Stability to non-zero frequency perturbations then places lower and upper bounds on the values of the remaining parameters. Second, we require that the exterior  $(\phi, |v|) = (-1, 0)$ , as well as being locally stable, also be the global minimum of the energy. This is ensured if the quadratic form defined by the derivative terms is positive definite. This generates a further inequality on one of the parameters. We do not describe these two calculations here due to lack of space, but the constraints are used in selecting parameters for the experiments. Third, we require that network configurations be stable. A network region consists of a set of branches, meeting at junctions. To analyse a general network configuration is very difficult, but if we assume that the branches are long and straight enough, then their stability can be analysed by

considering the idealized limit of a long, straight bar. The validity of this idealization will be tested using numerical experiments.

Ideally, the analysis should proceed by first finding the energy minimizing  $\phi_{R_{\text{Bar}}}$  and  $v_{R_{\text{Bar}}}$  for the bar region, and then expanding around these values. In practice, there are two obstacles. First,  $\phi_{R_{\text{Bar}}}$  and  $v_{R_{\text{Bar}}}$  cannot be found exactly. Second, it is not possible to diagonalize exactly the second derivative operator, and thus it is hard to impose positive definiteness for stability. Instead, we take simple *ansatzes* for  $\phi_{R_{\text{Bar}}}$  and  $v_{R_{\text{Bar}}}$  and study their stability in a low-dimensional subspace of function space. We define a four-parameter family of *ansatzes* for  $\phi_{R_{\text{Bar}}}$  and  $v_{R_{\text{Bar}}}$ , and analyse the stability of this family. Again, the validity of these *ansatzes* will be tested using numerical experiments. The first thing we need to do, then, is to calculate the energy of this idealized bar configuration.

### 3.1 Energy of the bar

Two phase field variables are involved: the scalar field  $\phi$  and the vector field  $v$ . The *ansatz* is as follows: the scalar field  $\phi$  varies linearly from  $-1$  to  $\phi_m$  across a region interface of width  $w$ , otherwise being  $-1$  outside and  $\phi_m$  inside the bar, which has width  $w_0$ ; the vector field  $v$  is parallel to the bar boundary, with magnitude that varies linearly from  $0$  to  $v_m$  across the region interface, otherwise being  $0$  outside and  $v_m$  inside the bar. The bar is thus described by the four physical parameters  $w_0$ ,  $w$ ,  $\phi_m$  and  $v_m$ .

To compute the total energy per unit length of the bar, we substitute the bar *ansatz* into Eq. (2) and (3). The result is

$$e_P(\hat{w}_0, \hat{w}, \phi_m, v_m) = \hat{w}_0 \nu(\phi_m, v_m) + \hat{w} \mu(\phi_m, v_m) - \beta(\phi_m + 1)^2 G_{00}(\hat{w}_0, \hat{w}) + \frac{\hat{D}(\phi_m + 1)^2 + \hat{L}_v v_m^2}{\hat{w}} \quad (5)$$

where  $\hat{w} = w/d$ ,  $\hat{w}_0 = w_0/d$ ,  $\hat{D} = D/d^2$  and  $\hat{L}_v = L_v/d^2$  are dimensionless parameters. The functions  $\mu$ ,  $\nu$  and  $G_{00}$  are given in appendix A. The parameters  $\mu$  and  $\nu$  play the same roles as  $\lambda$  and  $\alpha$  in the undirected network model given by Eq. (1). The energy gap between the foreground and the background is equal to  $2\alpha$  in the undirected network model and  $\nu$  in the directed network model, and  $\nu$  must be strictly positive to favour pixels belonging to the background. The parameter  $\mu$  controls the contribution of the region interface of width  $w$ : it has an effect similar to the parameter  $\lambda$ .

### 3.2 Stability of the bar

The energy per unit length of a network branch,  $e_P$ , is given by Eq. 5. A network branch is stable in the four-parameter family of *ansatzes* if it minimizes  $e_P$  with respect to variations of  $\hat{w}_0$ ,  $\hat{w}$ ,  $\phi_m$  and  $v_m$ . This is equivalent to setting the first partial derivatives of  $e_P$  equal to zero and requiring its Hessian matrix to be positive definite. The desired value of  $(\phi_m, v_m)$  is  $(1, 1)$  to describe the interior of the region  $R$ .

Setting the first partial derivatives of  $e_P$ , evaluated at  $(\hat{w}_0, \hat{w}, 1, 1)$ , equal to zero, and after some mathematical manipulation, one finds the following constraints:

$$\rho^* - G(\hat{w}_0, \hat{w}) = 0 \quad (6)$$

$$\beta = \frac{\nu^*}{4G_{10}(\hat{w}_0, \hat{w})} \quad (7)$$

$$\hat{D} = \frac{\hat{w}}{2} \left[ \frac{\nu^* G_{00}(\hat{w}_0, \hat{w})}{2G_{10}(\hat{w}_0, \hat{w})} - \hat{w} \mu_\phi^* \right] \quad (8)$$

$$\hat{L}_v = -\frac{\hat{w}^2 \mu_v^*}{2} \quad (9)$$

where  $G(\hat{w}_0, \hat{w}) = [G_{00}(\hat{w}_0, \hat{w})/\hat{w} + G_{11}(\hat{w}_0, \hat{w})]/G_{10}(\hat{w}_0, \hat{w})$ ,  $\rho^* = [\mu^* + \mu_\phi^* + \mu_v^*/2]/\nu^*$ ,  $\nu^* = \nu(1, 1)$ ,  $\mu^* = \mu(1, 1)$ ,  $\mu_\phi^* = \mu_\phi(1, 1)$  and  $\mu_v^* = \mu_v(1, 1)$ ;  $\mu_\phi = \partial\mu/\partial\phi_m$ ,  $\mu_v = \partial\mu/\partial v_m$ ,  $G_{10} = \partial G_{00}/\partial\hat{w}_0$  and  $G_{11} = \partial G_{00}/\partial\hat{w}$ . The starred parameters depend only on the 4 parameters of  $W$ :  $\pi_\lambda = (\lambda_{22}, \lambda_{21}, \lambda_{04}, \lambda_{03})$ . The conditions  $\hat{D} > 0$  and  $\hat{L}_v > 0$  generate lower and upper bounds on  $\hat{w}_0$ ,  $\hat{w}$  and  $\pi_\lambda$ .

Equation (6) shows that, for fixed  $\pi_\lambda$  i.e. when  $\rho^*$  is determined, the set of solutions in the plane  $(\hat{w}_0, \hat{w})$  is the intersection of the surface representing the function  $G$  and the plane located at  $\rho^*$ . The result is then a set of curves in the plane  $(\hat{w}_0, \hat{w})$  where each corresponds to a value of  $\rho^*$ . The top-left of Fig. 1 shows examples of solutions of Eq. (6) for some values of  $\rho^*$ . The solutions must satisfy the condition  $\hat{w} < \hat{w}_0$  otherwise the bar *ansatz* fails.

Equation (7) shows that bar stability depends mainly on the scaled parameter  $\hat{\beta} = \beta/\nu^*$ . The top-right of Fig. 1 shows a plot of  $\hat{\beta}$  against the scaled bar width  $\hat{w}_0$  and the scaled interface width  $\hat{w}$ . We have plotted the surface as two half-surfaces: one is lighter (left-hand half-surface, smaller  $\hat{w}_0$ ) than the other (right-hand half-surface, larger  $\hat{w}_0$ ). The valley between the half-surfaces corresponds to the minimum value of  $\hat{\beta}$  for each value of  $\hat{w}$ . The graph shows that: for each value  $\hat{\beta} < \hat{\beta}_{\min} = \inf(1/4G_{10}(\hat{w}_0, \hat{w})) = 0.0879$ , there are no possible values of  $(\hat{w}_0, \hat{w})$  which satisfy the constraints and so the bar energy does not have extrema; for each value  $\hat{\beta} > \hat{\beta}_{\min}$  and for some chosen value  $\hat{w}$ , there are two possible values of  $\hat{w}_0$  which satisfy the constraints: the smaller width (left-hand half-surface) corresponds to an energy maximum and the larger width (right-hand half-surface) corresponds to an energy minimum.

The second order variation of the bar energy is described by the  $4 \times 4$  Hessian matrix  $H$  which we do not detail due to lack of space. In order for the bar to be an energy minimum,  $H$  must be positive definite at  $(\hat{w}_0, \hat{w}, \phi_m, v_m) = (\hat{w}_0, \hat{w}, 1, 1)$ . This generates upper and lower bounds on the parameter values. This positivity condition is tested numerically because explicit expressions for the eigenvalues cannot be found.

The lower part of Fig. 1 shows the bar energy,  $e_P$ , plotted against the physical parameters of the bar  $\pi_B = (\hat{w}_0, \hat{w}, \phi_m, v_m)$ . The desired energy minimum was chosen at  $\pi_B^* = (1.36, 0.67, 1, 1)$ .<sup>1</sup> We choose a parameter setting,  $\pi_\lambda$ , and then compute  $D$ ,  $\beta$  and  $L_v$  using the parameter constraints given above. The bar energy per unit length  $e_P$  indeed has a minimum at the desired  $\pi_B^*$ .

<sup>1</sup> The parameter values were:  $(\lambda_{04}, \lambda_{03}, \lambda_{22}, \lambda_{21}, D, \beta, d, L_v, D_v) = (0.05, 0.025, 0.013, -0.6, 0.0007, 0.003, 1, 0.208, 0)$ .

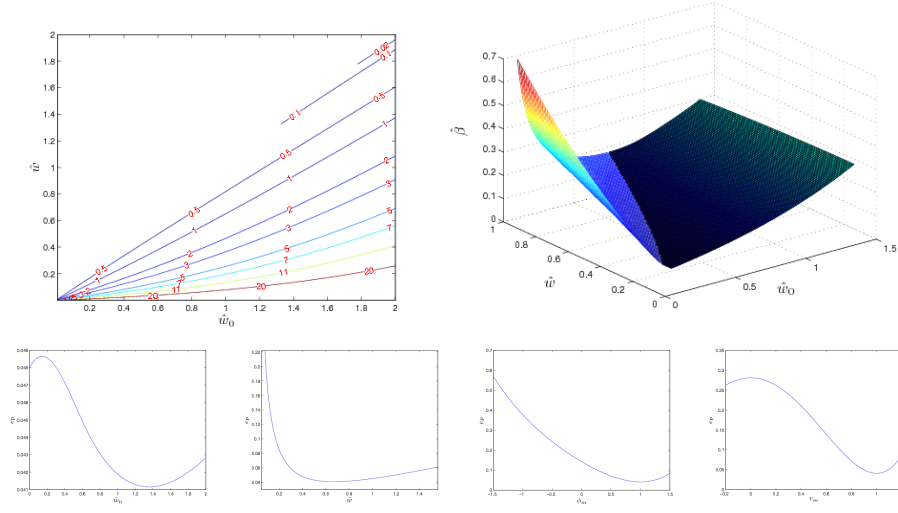


**Fig. 1.** Top-left: examples of solutions of Eq. (6) for some values of  $\rho^*$ ; curves are labelled by the values of  $\rho^*$ . Top-right: behaviour of  $\beta$ ; the light and dark surfaces show the locations of maxima and minima respectively. Bottom: bar energy  $e_P$  against the bar parameters  $\hat{w}$ ,  $\hat{w}_0$ ,  $\phi_m$  and  $v_m$ . Parameter values were chosen so that there is an energy minimum at  $\pi_B^* = (1.36, 0.67, 1, 1)$ .

### 3.3 Parameter settings in practice

There are nine free parameters in the model:  $(\lambda_{04}, \lambda_{03}, \lambda_{22}, \lambda_{21}, D, \beta, d, L_v, D_v)$ . Based on the stability analysis in Section 3, two of these parameters are eliminated while another two can be replaced by the ‘physical’ parameters  $\hat{w}_0$  and  $\hat{w}$ :  $(\lambda_{04}, \lambda_{03}, \lambda_{22}, \lambda_{21}, D_v, \hat{w}_0, \hat{w})$ . The interface width  $w$  should be taken as small as possible compatible with the discretization; in practice, we take  $2 < w < 4$  [9]. The desired bar width  $w_0$  is an application-determined physical parameter. We then fix the parameter values as follows: choose the 4 free parameter values  $(\lambda_{04}, \lambda_{03}, \lambda_{22}, \lambda_{21})$  of the ultralocal term  $W$ ; compute  $\nu^*$ ,  $\mu^*$ ,  $\mu_\phi^*$ ,  $\mu_v^*$  and then  $\rho^*$ , and solve Eq. (6) to give the values of the scaled widths  $\hat{w}_0$  and  $\hat{w}$ ; compute  $\beta$ ,  $\hat{D}$  and  $\hat{L}_v$  using the parameter constraints given by Eq. (7), (8) and (9), and then compute  $D = d^2 \hat{D}$  and  $L_v = d^2 \hat{L}_v$  where  $d = w_0/\hat{w}_0$ ; choose the free parameter  $D_v$ ; check numerically the stability of the phases  $(-1, 0)$  and  $(1, 1)$  as described briefly at the beginning of Section 3; check numerically positive definiteness of the Hessian matrix  $H$ .

## 4 Experiments

In Section 4.1, we present numerical experiments using the new model  $E_P$  that confirm the results of the theoretical analysis. In Section 4.2, we add a data likelihood and use the overall model to extract hydrographic networks from real images.



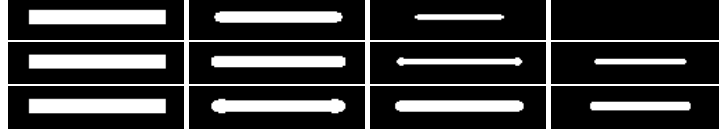


**Fig. 2.** Geometric evolutions of bars using the directed network model  $E_P$  with the interaction function  $K_0$ . Time runs from left to right. First column: initial configurations, which consist of a straight bar of width 10. The initial  $\phi$  is  $-1$  in the background and  $\phi_s$  in the foreground, and the initial vector field is  $(1, 0)$ . First row: when  $\hat{\beta} < \hat{\beta}_{\min}$ , the initial bar vanishes; second and third rows: when  $\hat{\beta} > \hat{\beta}_{\min}$ , the bars evolve toward bars which have the desired stable widths 3 and 6 respectively. The regions are obtained by thresholding the function  $\phi$  at 0.

#### 4.1 Geometric evolutions

To confirm the results of the stability analysis, we first show that bars of different widths evolve under gradient descent towards bars of the stable width predicted by theory. Fig. 2 shows three such evolutions.<sup>2</sup> In all evolutions, we fixed  $D_v = 0$ , because the divergence term cannot destabilize the bar when the vector field is initialized as a constant everywhere in the image domain. The width of the initial straight bar is 10. The first row shows that the bar evolves until it disappears because  $\hat{\beta} < \hat{\beta}_{\min}$ , so that the bar energy does not have a minimum for  $\hat{w}_0 \neq 0$ . On the other hand, the second and third rows show that straight bars evolve toward straight bars with the desired stable widths  $w_0 = 3$  and 6, respectively, when  $\hat{\beta} > \hat{\beta}_{\min}$ .

As a second test of the theoretical analysis, we present experiments that show that starting from a random configuration of  $\phi$  and  $v$ , the region evolves under gradient descent to a network of the predicted width. Fig. 3 shows two such evolutions.<sup>3</sup> At each point, the pair  $(\phi, |v|)$  was initialized randomly to be either  $(-1, 0)$  or  $(1, 1)$ . The orientation of  $v$  was chosen uniformly on the circle. The evolutions in the first row has predicted stable width  $w_0 = 5$ , while that in the second row has predicted stable width  $w_0 = 8$ . In all cases, the initial configuration evolves to a stable network region with branch widths equal to the predicted value, except near junctions, where branch width changes significantly to accommodate flow conservation.

#### 4.2 Results on real images

In this section, we use the new model to extract hydrographic networks from multi-spectral VHR Quickbird images. The multi-spectral channels are red, green, blue and infra-red. Fig. 4 shows three such images in which parts of the hydrographic network to be extracted are obscured in some way.

<sup>2</sup> From top to bottom, parameter values were:  $(\lambda_{04}, \lambda_{03}, \lambda_{22}, \lambda_{21}, D, \beta, d, L_v, D_v) = (0.1, -0.064, 0.232, -0.6, 0.065, 0.0027, 3.66, 0.5524, 0)$ ,  $(0.112, 0.019, -0.051, -0.6, 0.055, 0.011, 2.78, 0.115, 0)$  and  $(0.1, -0.064, 0.232, -0.6, 0.065, 0.0077, 3.66, 0.5524, 0)$ .

<sup>3</sup> From top to bottom, the parameter values were:  $(\lambda_{04}, \lambda_{03}, \lambda_{22}, \lambda_{21}, D, \beta, d, L_v, D_v) = (0.25, 0.0625, 0.0932, -0.8, 0.111, 0.0061, 3.65, 0.0412, 50)$  and  $(0.4, -0.1217, 0.7246, -1, 0.4566, 0.0083, 10.8, 0.4334, 100)$ .

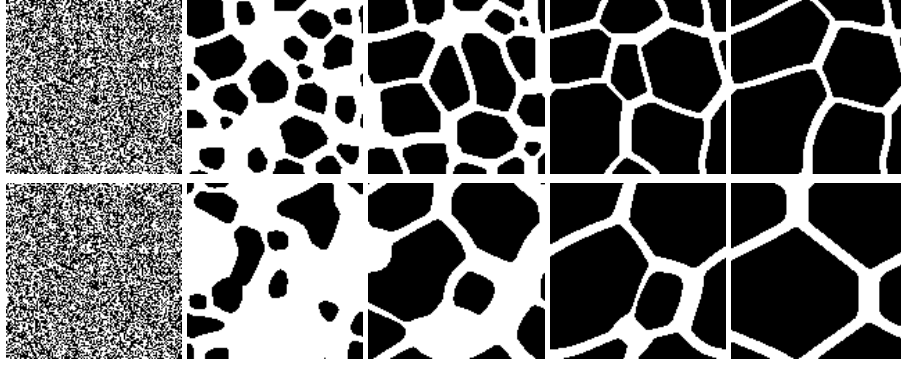


**Fig. 3.** Geometric evolutions starting from random configurations. Time runs from left to right. Parameter values were chosen as a function of the desired stable width, which was 5 for the first row and 8 for the second row. Both initial configurations evolve towards network regions in which the branches have widths equal to the predicted stable width, except near junctions, where branch width changes significantly to accommodate flow conservation. The regions are obtained by thresholding the function  $\phi$  at 0.

To apply the model, a likelihood energy linking the region  $R$  to the data  $I$  is needed in addition to the prior term  $E_P$ . The total energy to minimize is then  $E(\phi, v) = \theta E_P(\phi, v) + E_I(\phi)$  where the parameter  $\theta > 0$  balances the two energy terms. The likelihood energy  $E_I(\phi)$  is taken to be a multivariate mixture of two Gaussians (MMG) to take into account the heterogeneity in the appearance of the network produced by occlusions. It takes the form

$$E_I(\phi) = -\frac{1}{2} \int_{\Omega} dx \left\{ \ln \sum_{i=1}^2 p_i |2\pi \Sigma_i|^{-1/2} e^{-\frac{1}{2} (I(x) - \mu_i)^t \Sigma_i^{-1} (I(x) - \mu_i)} - \ln \sum_{i=1}^2 \bar{p}_i |2\pi \bar{\Sigma}_i|^{-1/2} e^{-\frac{1}{2} (I(x) - \bar{\mu}_i)^t \bar{\Sigma}_i^{-1} (I(x) - \bar{\mu}_i)} \right\} \phi(x) \quad (10)$$

where the parameters  $(p_1, p_2, \bar{p}_1, \bar{p}_2, \mu_1, \mu_2, \bar{\mu}_1, \bar{\mu}_2, \Sigma_1, \Sigma_2, \bar{\Sigma}_1, \bar{\Sigma}_2)$  are learnt from the original images using the Expectation-Maximization algorithm; labels 1 and 2 refer to the two Gaussian components and the unbarred and barred parameters refer to the interior and exterior of the region  $R$  respectively;  $^t$  indicates transpose.

Fig. 4 shows the results. The second row shows the maximum likelihood estimate of the network (*i.e.* using the MMG without  $E_P$ ). The third and fourth rows show the MAP estimates obtained using the undirected network model,<sup>4</sup>  $E_P^s$ , and the directed network model,<sup>5</sup>  $E_P$ , respectively.

<sup>4</sup> The parameter values were, from left to right:  $(\lambda, \alpha, D, \beta, d) = (18.74, 0.0775, 11.25, 0.0134, 34.1), (4.88, 0.3327, 3, 0.0575, 4.54)$  and  $(19.88, 0.6654, 12, 0.1151, 9.1)$ .

<sup>5</sup> The parameter values were, from left to right:  $(\lambda_{04}, \lambda_{03}, \lambda_{22}, \lambda_{21}, D, \beta, d, L_v, D_v, \theta) = (0.412, -0.0008, 0.0022, -0.6, 0.257, 0.0083, 8.33, 0.275, 50, 25), (0.2650, -0.1659,$

		Completeness = TP / (TP+FN)	Correctness = TP / (TP+FP)	Quality = TP / (TP+FP+FN)
1	UNM	0.8439	0.9168	0.7739
	DNM	0.8202	0.9489	<b>0.7924</b>
2	UNM	0.9094	0.6999	0.6043
	DNM	0.8484	0.7856	<b>0.6889</b>
3	UNM	0.5421	0.6411	0.4158
	DNM	0.7702	0.6251	<b>0.6513</b>

**Table 1.** Quantitative evaluations of experiments of the three images given in Fig. 4. T, F, P, N, UNM and DNM correspond to true, false, positive, negative, undirected network model and directed network model respectively.

The undirected network model favours network structures in which all branches have the same width. Consequently, network branches which have widths significantly different from the average are not extracted. The result on the third image shows clearly the false negative in the central part of the network branch, where the width is about half the average width. Similarly, the result on the second image shows a false positive at the bottom of the central loop of the network, where the true branch width is small. The result on the first image again shows a small false negative piece in the network junction at the bottom.

The directed network model remedies these problems, as shown by the results in the fourth row. The vector field was initialized to be vertical for the first and third images, and horizontal for the second image.  $\phi$  and  $|v|$  are initialized at the saddle point of the ultralocal term  $W$ , except for the third image where  $|v| = 1$ . The third image shows many gaps in the hydrographic network due mainly to the presence of trees. These gaps cannot be closed using the undirected network model. The directed network model can close these gaps because flow conservation tends to prolong network branches. See Table 1 for quantitative evaluations.

## 5 Conclusion

In this paper, we have conducted a theoretical study of a phase field HOAC model of directed networks in order to ascertain parameter ranges for which stable networks exist. This was done via a stability analysis of a long, straight bar that enabled some model parameters to be fixed in terms of the rest, others to be replaced by physically meaningful parameters, and lower and upper bounds to be placed on the remainder. We validated the theoretical analysis via numerical experiments. We then added a likelihood energy and tested the model on the problem of hydrographic network extraction from multi-spectral VHR satellite images, showing that the directed network model outperforms the undirected network model.

---

0.5023,  $-0.8$ , 0.1926, 0.0387, 2.027, 0.2023, 100, 16.66) and (0.4525,  $-0.2629$ , 0.6611,  $-0.8$ , 0.3585, 0.0289, 5.12, 0.4224, 10, 22.22).

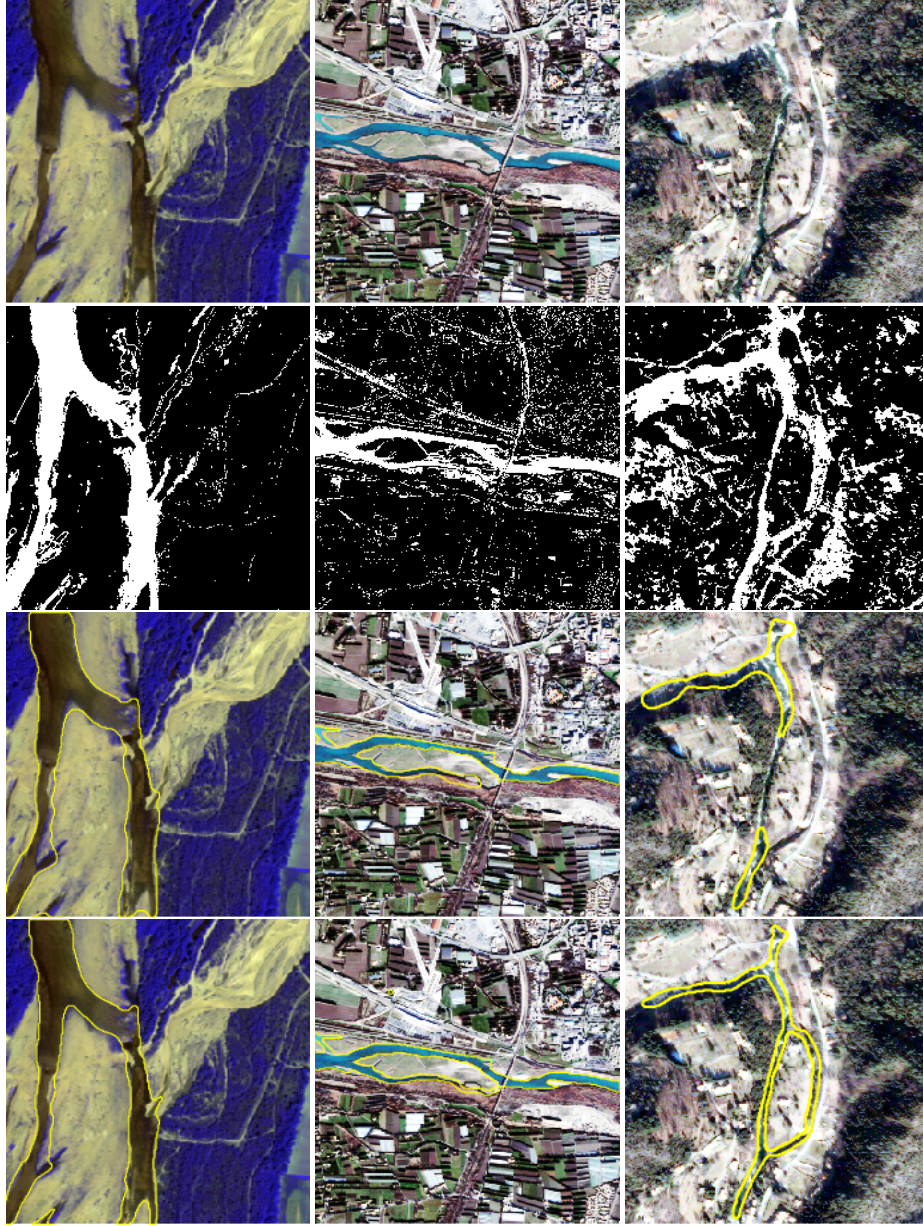


**Fig. 4.** From top to bottom: multispectral Quickbird images; ML segmentation; MAP segmentation using the undirected model  $E_P^s$ ; MAP segmentation using the directed model  $E_P$ . Regions are obtained by thresholding  $\phi$  at 0. (Original images ©DigitalGlobe, CNES processing, images acquired via ORFEO Accompaniment Program).

## A Appendix

The functions  $\mu$ ,  $\nu$  and  $G_{00}$  are

$$\begin{aligned} \mu = & -\frac{3v_m^4}{20} + \frac{v_m^2}{2} \left( \frac{\lambda_{22}}{10}(\phi_m + 1)(-3\phi_m + 2) + \frac{\lambda_{21}}{6}(-3\phi_m + 1) + \frac{1}{3} \right) \\ & + \frac{\lambda_{04}}{60}(\phi_m + 1)^2(-9\phi_m^2 + 12\phi_m + 1) + \frac{\lambda_{03}}{6}(\phi_m + 1)^2(-\phi_m + 1) \\ & + \frac{1}{24}(\lambda_{22} + \lambda_{21})(\phi_m + 1)^2 \end{aligned} \quad (11)$$

$$\begin{aligned} \nu = & \frac{v_m^4}{4} + \frac{v_m^2}{2} \left( \frac{\lambda_{22}}{2}(\phi_m^2 - 1) + \lambda_{21}(\phi_m - 1) - 1 \right) + \frac{\lambda_{04}}{4}(\phi_m^2 - 1)^2 \\ & + \frac{\lambda_{03}}{3}(\phi_m + 1)^2(\phi_m - 2) - \frac{1}{8}(\lambda_{22} + \lambda_{21})(\phi_m + 1)^2 \end{aligned} \quad (12)$$

$$G_{00} = \frac{2}{\hat{w}^2} \int_0^{+\infty} \int_0^{\hat{w}} dz dx_2 \int_{-x_2}^{\hat{w}-x_2} dt \Psi(\sqrt{z^2 + t^2}) - \Psi(\sqrt{z^2 + (\hat{w}_0 + t)^2}) \quad (13)$$

**Acknowledgement.** The authors thank the French Space Agency (CNES) for the satellite images, and CNES and the PACA Region for partial financial support.

## References

1. Chen, Y., Tagare, H., Thiruvankadam, S., Huang, F., Wilson, D., Gopinath, K., Briggs, R., Geiser, E.: Using prior shapes in geometric active contours in a variational framework. *IJCV* **50** (2002) 315–328
2. Cremers, D., Kohlberger, T., Schnörr, C.: Shape statistics in kernel space for variational image segmentation. *Pattern Recognition* **36** (2003) 1929–1943
3. Paragios, N., Rousson, M.: Shape priors for level set representations. In: *ECCV*, Copenhagen, Denmark (2002)
4. Srivastava, A., Joshi, S., Mio, W., Liu, X.: Statistical shape analysis: Clustering, learning, and testing. *IEEE Trans. PAMI* **27** (2003) 590–602
5. Riklin Raviv, T., Kiryati, N., Sochen, N.: Prior-based segmentation and shape registration in the presence of perspective distortion. *IJCV* **72** (2007) 309–328
6. Taron, M., Paragios, N., Jolly, M.P.: Registration with uncertainties and statistical modeling of shapes with variable metric kernels. *IEEE Trans. PAMI* **31** (2009) 99–113
7. Vaillant, M., Miller, M.I., Younes, A.L., D, A.T.: Statistics on diffeomorphisms via tangent space representations. *NeuroImage* **23** (2004) 161–169
8. Rochery, M., Jermyn, I., Zerubia, J.: Higher order active contours. *IJCV* **69** (2006) 27–42
9. Rochery, M., Jermyn, I.H., Zerubia, J.: Phase field models and higher-order active contours. In: *ICCV*, Beijing, China (2005)
10. El Ghouli, A., Jermyn, I.H., Zerubia, J.: A phase field higher-order active contour model of directed networks. In: *NORDIA*, in conjunction with *ICCV*, Kyoto, Japan (2009)
11. El Ghouli, A., Jermyn, I.H., Zerubia, J.: Segmentation of networks from VHR remote sensing images using a directed phase field HOAC model. In: *ISPRS / PCV*, Paris, France (2010)
12. El Ghouli, A., Jermyn, I.H., Zerubia, J.: Phase diagram of a long bar under a higher-order active contour energy: application to hydrographic network extraction from VHR satellite images. In: *ICPR*, Tampa, Florida (2008)